## Properties of Silicon-Added, Iron-Based, Slag-Free, Self-Shielded Flux-Cored Wire

The addition of silicon to the iron-based hardfacing alloy improved the wear resistance owing to the higher hardness and refinement of the microstructure

BY D. S. LIU AND P. WEI

### **ABSTRACT**

In this investigation, a new type of silicon-added, slag-free, self-shielded fluxcored wire was developed. Silicon had a high affinity for oxygen and was easily oxidized to change the pore formation tendency, and the residual silicon element affected the microstructure during the following solidification process. The results showed that silicon up to 12 wt-% reduced the formation of the CO gas, resulting in the absence of the weld pool boiling, thus leading to weld porosity. The Si-free hardfacing alloy displayed a typical hypereutectic microstructure that consisted of primary hexagonal-shaped M<sub>7</sub>(C, B)<sub>3</sub> and eutectic colonies of M<sub>3</sub>(C, B) plus austenite. With increasing the amount of silicon additive, the primary M<sub>7</sub>(C, B)<sub>3</sub> carbides gradually refined and became more uniform. The ferrite was formed directly from the liquid in the silicon-added hardfacing alloy. Fe<sub>3</sub>Si was formed when the silicon concentration in the residual liquid reached a certain level (the alloy with 12 wt-% silicon additive). The addition of silicon to the iron-based hardfacing alloy improved the wear resistance owing to the higher hardness and refinement of the microstructure. The iron-based, slag-free, self-shielded flux-cored wire offered the best combination of the properties when 12 wt-% silicon was added to the core.

#### **KEYWORDS**

- Silicon Additive Iron Base Self-Shielded Flux-Cored Wire Hardfacing
- Wear Resistance Weld Porosity

### Introduction

High-chromium, iron-based hardfacing alloys have been widely used to achieve longer service life for the wearresistant parts of steel rolling and mineral pulverizing mills (Refs. 1–3). Their excellent wear resistance is attributed to the presence of a large volume fraction of  $M_7C_3$  carbides in the microstructure (Refs. 4–6). The alloys are usually accomplished by welding technology, such as shielded metal arc, gas metal arc, submerged arc, and selfshielded flux-cored arc welding (Refs.

7, 8). Among these methods, selfshielded flux-cored arc welding has the highest values of deposition rate, which is particularly important for regeneration of heavy working surfaces (Refs. 9-11).

Self-shielded flux-cored wires are generally composite tubular filler metal electrodes having a metal tube and a core composition of various welding fluxes. In the absence of any inert shielding gas for protecting the arc and the molten pool, the self-shielding ability of the wire requires amounts of fluxing agents, which form slag on the

deposit in the welding process (Refs. 12, 13). Unfortunately, the fluxing agents, such as marble, rutile, and fluorite, occupy more screen space because of their lesser density compared to the metal powders. The addition of ferroalloys, such as ferrochrome, is restricted. The M<sub>7</sub>C<sub>3</sub> carbides are insufficient in the microstructure of hardfacing, mainly due to the addition difficulties of ferroalloys in the core.

Thus, we have developed a new slag-free type of iron-based, selfshielded flux-cored wires (Refs. 14-16). The slag-free, self-shielded flux-cored wires have a core composition comprised primarily of metal powders with substantially reduced amounts of fluxing agents. To reduce the pore formation tendency, strong deoxidizers like silicon were added into the core to protect the weld metal. Here, the effects of silicon on the pore sensitivity, microstructure, and wear resistance of iron-based, slagfree, self-shielded flux-cored wires were investigated.

### **Experimental Procedures**

During the manufacture of slagfree, self-shielded flux-cored wires, the core composition was blended and deposited onto a steel strip (H08A steel: 16 mm in width and 0.3 mm in thickness), which was formed into a tube, about the core composition (containing ferrosilicon, high-carbon ferrochrome, graphite, and electrolytic manganese, etc.) in a forming mill.

D. S. LIU (hardfacing@163.com) is with School of Material Science and Engineering, Jiangsu University of Science and Technology, Zhenjiang, China. P. WEI is with School of Naval Architecture & Ocean Engineering, Jiangsu University of Science and Technology, Zhenjiang, China.

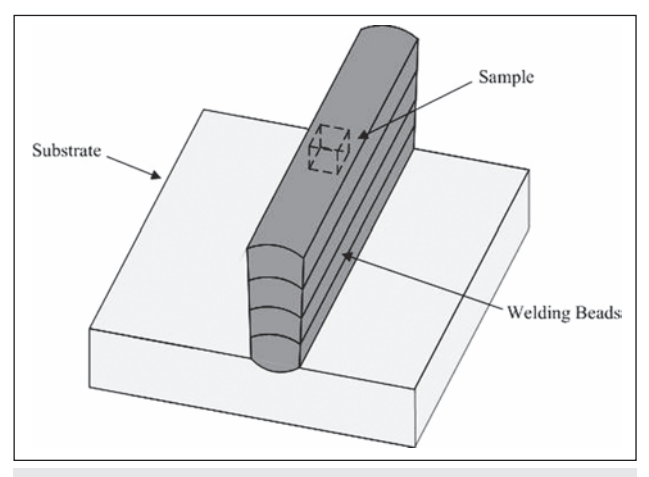


Fig. 1 — Schematic illustration of hardfacing.



Fig. 2 — Typical weld appearance of the hardfacing alloy deposited by slag-free, self-shielded flux-cored wire.



Fig. 3 — Effect of silicon on porosity of the hard-facing alloy.



The steel tube surrounding the core composition was then drawn through reducing dies to a specified wire diameter (2.8 mm). The chemical composition of the steel sheath is shown in Table 1, and the composition of the powdery metal-core fill within the

 ${\it Table 1-Composition of Steel Sheath}\\$ 

C	≤0.12
Si	≤0.04
Mn	≤0.50
Р	≤0.035
S	≤0.035

steel sheath (filling rate: 55 wt-%) is shown in Table 2. In order to investigate the effects of silicon additive on the properties of iron-based, selfshielded flux-cored hardfacing alloys, the mass fraction of Fe-Si (containing 75 wt-% Si) added into the core wire was 0, 6, 12, 18, and 24 wt-%.

Figure 1 shows a schematic illustration of hardfacing. Mild steel with the dimensions of  $150 \times 75 \times 50$  mm was selected as the substrate material. In order to obtain the homogeneous specimen, hardfacing alloys with four layers were prepared by means of slag-

free, self-shielded flux-cored arc welding without preheat and postheat. The welding parameters are presented in Table 3.

Samples with dimensions of  $10 \times$ 10 × 8 mm were cut from the top welding beads (see Fig. 1). The samples were cleaned in an ultrasonic cleaning machine for 5 min before and after the test. The hardness was taken on the top surface of the hardfacing alloys by an HR-150A Rockwell hardness tester. The chemical compositions of the hardfacing alloys were analyzed by a SPECTRO MAXx LAB optical emission spectrograph (OES). The etching agent was composed of 15 mL of 38% hydrochloric acid solution, 50 mL H<sub>2</sub>O, 3 mL of 68% nitric acid solution, and 3 g ferric chloride. The microstructures were observed by optical microscope (OM) and scanning electron microscope (SEM). Twenty randomly selected regions with areas of 16 × 16 mm were used for image analysis to determine the carbide diameter in microstructures of hardfacing alloys with varying Fe-Si content.

Abrasion testing was carried out using a UMT-2 pin on disc wear test machine. The parameters of the wear test are summarized in Table 4. The corresponding friction coefficient was gotten from the ratio of the friction force to the applied load. The wear loss, V, was determined using the following equation:

$$V = 2\pi r S \tag{1}$$

where *r* is the wear track radius, and *S* is the cross-sectional areas of the wear track determined by a data visualiza-

 ${\bf Table~2-Composition~of~the~Flux~Core}$ 

Content				
(wt-%)				
No. 1	No. 2	No. 3	No. 4	No. 5
0	6	12	18	24
58.5	58.5	58.5	58.5	58.5
3	3	3	3	3
1	1	1	1	1
10	10	10	10	10
3.5	3.5	3.5	3.5	3.5
24	18	12	6	0
	0 58.5 3 1 10 3.5	No. 1 No. 2 0 6 58.5 58.5 3 3 1 1 10 10 3.5 3.5	No. 1         No. 2         No. 3           0         6         12           58.5         58.5         58.5           3         3         3           1         1         1           10         10         10           3.5         3.5         3.5	(wt-%)       No. 1     No. 2     No. 3     No. 4       0     6     12     18       58.5     58.5     58.5     58.5       3     3     3       1     1     1     1       10     10     10     10       3.5     3.5     3.5

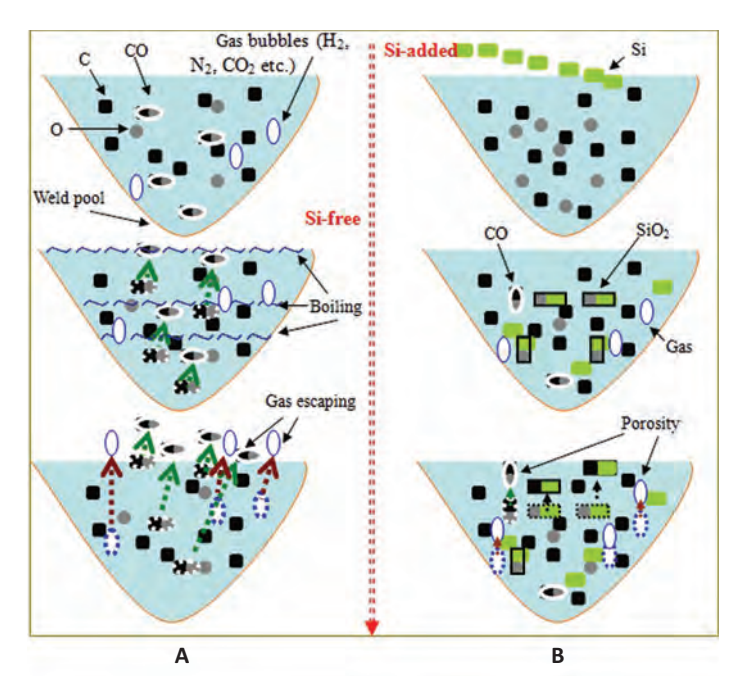


Fig. 4 — The mechanism of porosity of slag-free, self-shielded flux-cored wires: A — Without silicon additive; B — with silicon additive.

tion and analysis tool Gwyddion 2.39. Three testing specimens were made from each sample and were tested separately. An average of the three numbers was calculated and recorded. The wear tracks were observed by Gwyddion 2.39.

### **Results and Discussion**

# Effect of Silicon on Porosity of the Alloy

Figure 2 shows the typical surface appearance of hardfacing deposited by using slag-free, self-shielded flux-cored wires. The hardfacing alloys show good surface appearance without the presence of cracks or slags. Figure 3 shows the changes of pore sensitivity of the hardfacing with the percentage change of silicon powder in the core of the wire. With the silicon content increasing from 0 to 12 wt-%, there was no porosity observed in the hardfacing alloy. However, porosity appeared when the silicon content reached 18 wt-%. When the silicon content was 24 wt-%. the porosity of the alloy was relatively severe compared to the porosity of the alloy with 18 wt-% silicon, and porosity in the form of large discontinuous cavities or long continuous holes occurred as shown in Fig. 3B.

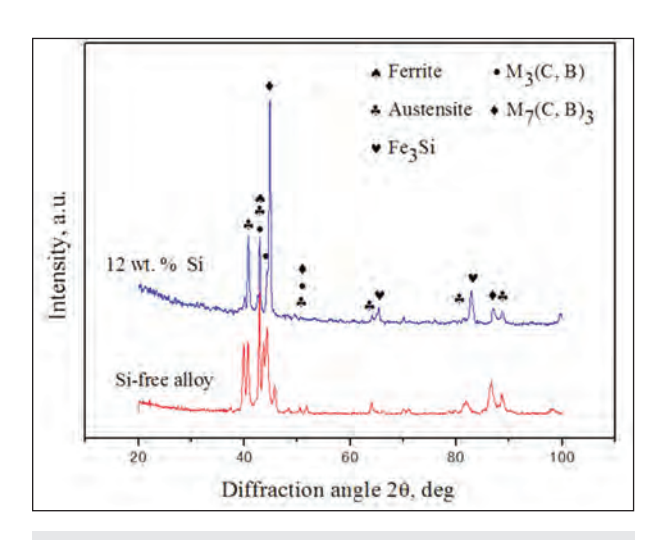


Fig. 5 — XRD of hardfacing alloy with different silicon additions.

Figure 4A shows the mechanism of porosity prevented with slag-free, self-

shielded flux-cored wires. The addition of deoxidizers such as graphite (C), magaluma (Al, Mg), manganese (Mn), and ferrosilicon (Fe-Si) in the filler metal helps reduce the amount of porosity. Since Al and Mg are better deoxidants than the others, they reduce the oxidizability of the welding atmosphere at an earlier stage of deoxidization. The reaction formulas of deoxidization are

$$2Al + 3O = Al_2O_3$$
 (2)

$$Mg + O = MgO$$
 (3)

Moreover, at the latter deoxidization (mainly in the weld pool), the reaction formulas of deoxidization are

$$Mn + O = MnO$$
 (4)

$$Si + 2O = SiO_2$$
 (5)

$$C + O = CO (6)$$

Large amounts of CO gas resulting from a chemical reaction (Equation 6) bring the weld pool to the boil owing to their intense escape from the pool. Thus, the gas bubbles ( $H_2$ ,  $N_2$ ,  $CO_2$ , etc.) escape from the boiling weld pool easily. The hardfacing alloys deposited by slagfree, self-shielded flux-cored wires are

practically porosity free.

Figure 4B shows the mechanism for silicon to increase pore sensitivity. With increasing Si content, the oxygen concentration decreases in the weld pool, as would be expected from Equation 5. It prevents the formation of large amounts of CO gas (Equation 6). When the silicon content exceeded 18 wt-%, the CO concentration was not enough to keep the weld pool boiling. The bubbles rose in the weld pool more slowly. Under high cooling speeds, gas bubbles that do not have enough time to leave deep weld pools result in weld porosity.

Moreover, silicon is well known to promote ferrite. Ferrite has orders of magnitude less soluble for nitrogen than does austenite. The ferrite was formed directly from the liquid in the silicon-added hardfacing alloy (see Fig. 5); the porosity was also expected.

Porosity results and analyses discussed previously suggest that the ideal content of Si was less than or equal to 12 wt-%. The residual silicon element affected the microstructure during the following solidification process.

# Effect of Silicon on the Alloy Microstructure

Table 5 shows the chemical compositions of the hardfacing alloys. With the increase of silicon additive in the wire, the silicon content increased in the hardfacing alloy.

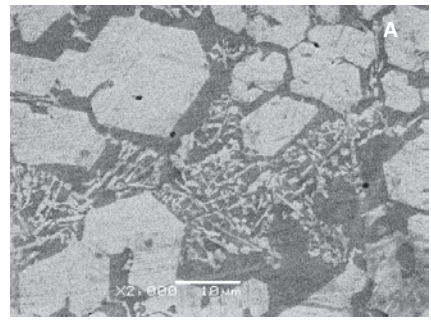
Figure 5 shows the XRD pattern of the hardfacing alloys. The phase in the

Si-free hardfacing alloy was mainly composed of  $(Cr, Fe)_7(C, B)_3$ ,  $Fe_3(C, B)$ , and austenite. The figure also shows the presence of ferrite and  $Fe_3Si$  in the hardfacing alloy with silicon addition (e.g., the alloy containing 12 wt-% Fe-Si).

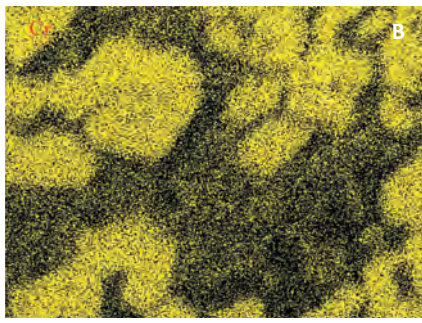
The distribution of silicon, chromium, and manganese is illustrated in Fig. 6. Figure 6B shows chromium was detected in the precipitations with white color while manganese was mainly detected in these precipitations — Fig. 6C. It was identified that the white precipitations were Cr-rich Mnrich carbides. In addition, silicon was detected into the matrix but not  $M_7(C,$ B)<sub>3</sub> carbides — Fig. 6D. Accompanying the formation of the primary  $M_7(C,$ B)<sub>3</sub> carbides, the residual liquid was enriched in carbon, Fe, Si, B, and C. The eutectic of austenite plus  $Fe_3(C, B)$ and Fe<sub>3</sub>Si was subsequently formed when the silicon concentration in the residual liquid reached a certain level.

Furthermore, changing the silicon content altered the microstructure, as illustrated in Fig. 7. As shown in Fig. 7A, the Si-free hardfacing alloy displays a typical hypereutectic microstructure that consisted of primary hexagonal-shaped M<sub>7</sub>(C, B)<sub>3</sub> and eutectic colonies of M<sub>3</sub>(C, B) plus martensite and residual austenite as determined by XRD analysis. With increase in the amount of silicon additive (Fig. 7B, C), the primary  $M_7(C, B)_3$  carbides gradually refined and became more uniform. Figure 8 displays the change of average diameter of the  $M_7(C, B)_3$ carbides with different silicon contents. The average carbide diameter was the largest in the Si-free alloy (17.8 um) followed by that in alloys with 6 wt-% silicon (13.2 um) and alloys with 12 wt-% silicon (8.6 um). It indicates the carbide size gets smaller with the increase in the silicon content in the hardfacing alloy. Similar results were found in the high-strength steels (Ref. 17).

Figure 9 shows the EDS results of matrix of hardfacing alloys with various silicon contents. The matrix of silicon-free hardfacing alloy consisted of 13.7 wt-% Cr as shown in Fig. 9A. Moreover, when the Fe-Si additive was 6 wt-%, the Si and Cr contents were 6.15 and 12.32 wt-%, respectively — Fig. 9B. When the Fe-Si additive was 12 wt-%, the Si and Cr contents changed to 13.54 and 4.55 wt-%, re-







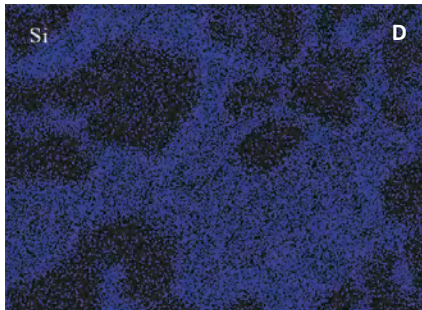


Fig. 6 — EPMA area analysis for silicon-added alloy: A — Overall image; B-D — Cr, Si, Mn distribution.

Table 3 — Welding Parameters

Process parameter	Constant value		
Welding current (A) Arc voltage (V) Electrode polarity	440–460 32–34 positive		
Welding speed (m min-1)	0.3		
Stickout (mm)	25-32		
Electrode angle to plate surface (deg)	10		

Table 4 —	Sliding	Wear	Test	Conditions

Parameter	Value
Counterface Material	$Al_2O_3$
Load (N)	10
Velocity (rev/min)	560
Wear time (min)	20
Diameters of the ball (mm)	3
Radius of wear track (mm)	4

spectively — Fig. 9C. Therefore, the effect of silicon was to increase the level of silicon but reduce the level of chromium in the matrix. The decrease in the chromium content of the matrix formed should, in fact, be beneficial since chromium was best used in forming hard  $M_7(C, B)_3$  carbides during earlier solidification.

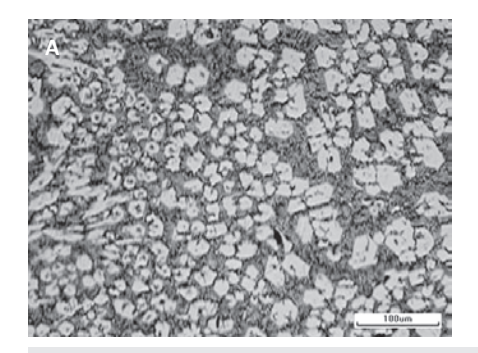
Figure 10 shows the SEM images of hardfacing alloys with various silicon contents. As seen in Fig. 10A, there was a typical hypereutectic structure in the silicon-free alloy. During the solidification process, the primary hexagonal  $M_7(C,B)_3$  carbides were formed in the high-temperature weld pool, followed by the eutectic reaction. The eutectic colonies consisted of long bar-like eutectic carbides plus austenite matrix. In alloys with 6 wt-% silicon, the eutectic carbides were the scattered web form — Fig. 10B.

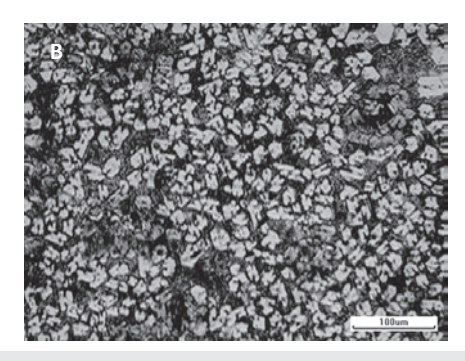
Figure 11 shows the EDS spectrum of a small strip of particles in the mi-

crostructure of the alloy with 12 wt-% silicon (see the red arrow in Fig. 10C). The atomic ratio between Fe and Si was about 3:1; therefore, the Fe-Si phase was highly likely corresponding to the Fe<sub>3</sub>Si in the phase diagram (Ref. 18). This was confirmed by XRD analysis, as shown in Fig. 5. The Fe<sub>3</sub>Si was also found in the GTAW cladding alloyed on the St52 steel with preplaced 45 Fe-39 Cr-6C-10Si powders (Ref. 19).

### Effect of Silicon Addition on Alloy Hardness and Wear Resistance

Figure 12 shows the effect of silicon on the hardness and wear resistance of hardfacing alloys. It can be seen that the hardness was increased steadily with the increase in silicon content. The hardness of the silicon-free alloy was 58.8 HRC and increased to 62.7





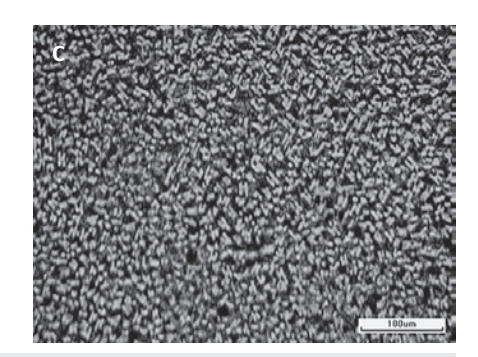


Fig. 7 — Microstructures of hardfacing alloys with different silicon additions: A = 0 wt-%; B = 6 wt-%; C = 12 wt-%.

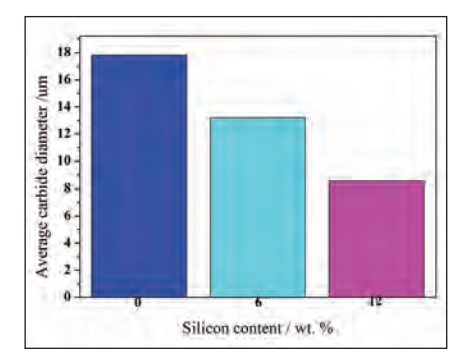


Fig. 8 — The change in average diameter of the M<sub>7</sub>(C, B)<sub>3</sub> carbides with different silicon contents.

HRC when adding 12 wt-% silicon. Solid solution of silicon in the matrix was beneficial to the hardness. With the increase in silicon content, the formation of more refined  $M_7(C, B)_3$  carbides also led to the increase in bulk hardness. Furthermore, the wear loss decreased with an increase in the silicon in the wire. This improved wear resistance was attributed to the formation of hard M<sub>7</sub>(C, B)<sub>3</sub> carbides in the microstructure of the solid solution (Fe, Cr, Mn, Si) and also to the significant microstructural refinement.

The friction coefficient was measured automatically during wear tests, and the results are plotted in Fig. 13. The friction coefficients of the siliconadded hardfacing alloys were less than that of the silicon-free hardfacing alloy. This can be attributed to the high hardness of the silicon-added hardfacing alloy that resulted in a small real area of contact, thus, the smaller number of junctions required less energy to be sheared during sliding than the siliconfree hardfacing alloy. Moreover, the tough matrix through hardenability and the refinement microstructure reduced the adhesion in the wear process.

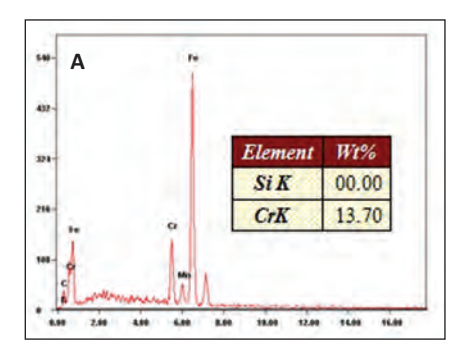
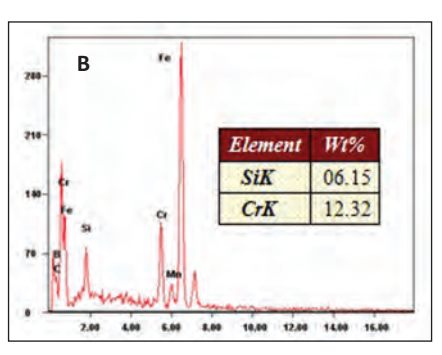


Figure 14 shows the worn surface after the sliding wear test. The worn surface of the silicon-free alloy was easily plastically deformed and grooved, and the wear behavior was featured as abrasive and adhesive wear — Fig. 14A. As can be seen, the worn surface of the alloy with 12 wt-% silicon was characterized by the presence of shallower grooves and slighter adhesive features (Fig. 14C) than that of the alloy with 6 wt-% silicon (Fig. 14B) and silicon-free alloy — Fig. 14A. It indicates the alloy with 12 wt-% silicon additive displayed the best wear resistance.

The microstructure of the hardfacing alloys consisted of austenite with  $M_7(C, B)_3$  carbides,  $M_3(C, B)$  carbides, or Fe<sub>3</sub>Si particles. In general, the two phases of the wear-resistant materials served different functions: the hard  $M_7(C, B)_3$  carbides and  $M_3(C, B)$  carbides were to impede wear by grooving or indenting mineral particles, while the matrix was meant to provide suffi-



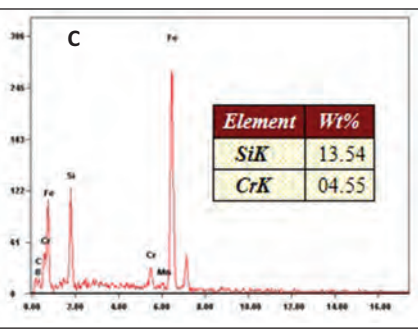


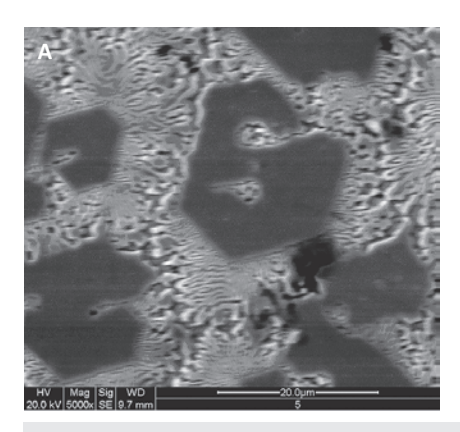
Fig. 9 — The level of silicon and chromium in the matrix of hardfacing alloys with different silicon additions.

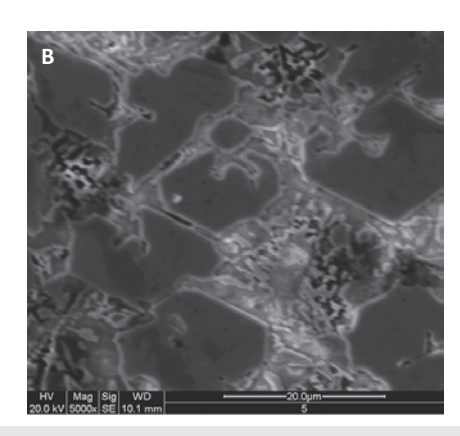
cient toughness. Both properties depended on the amount, size, and distribution of the hard carbides as well as on the hardness and fracture toughness of both constituents and the bond between them.

A major effect of silicon was to refine the morphology of the primary  $M_7(C,$ B)<sub>3</sub> carbides. This morphological refinement should be beneficial to the tough-

Table 5 — Chemical Compositions of the Hardfacing Alloys (wt-%)

Specimen (Fe-Si additive)	Si	С	В	Cr	Mn	Fe
0	0	2.70	0.89	19.28	1.21	Bal.
6	2.14	2.79	0.92	18.59	1.16	Bal.
12	4.32	2.92	0.90	18.37	1.24	Bal.





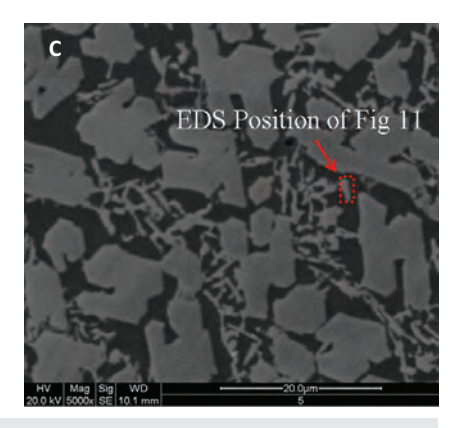


Fig. 10 - SEM images of hardfacing alloys with different silicon additions: A - Silicon-free; B - 6 wt-% silicon; C - 12 wt-% silicon.

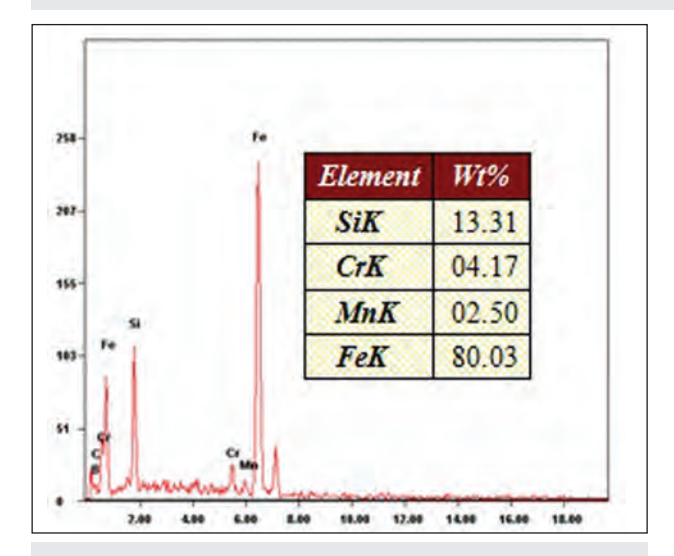


Fig. 11 — The EDS spectrum of a small strip of particles in the microstructure of the alloy with 12 wt-% silicon.

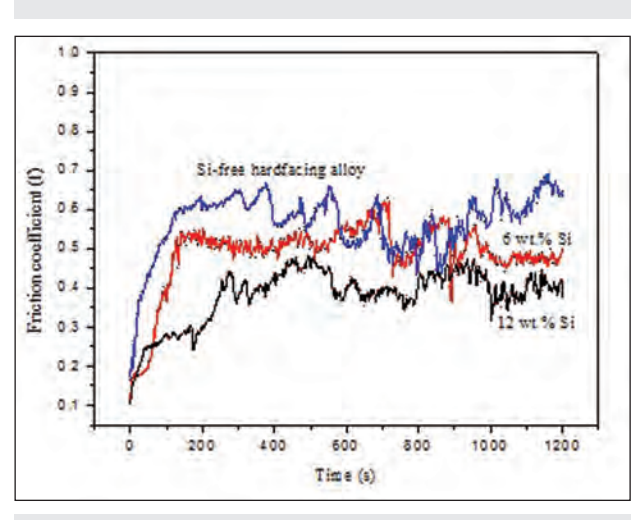


Fig. 13 — The friction coefficient vs. sliding time for the hardfacing alloy with different silicon additions.

ness of the alloy, perhaps imparting better abrasion wear resistance, and in fact, experiments are in progress to confirm this. The effect of silicon was also to in-

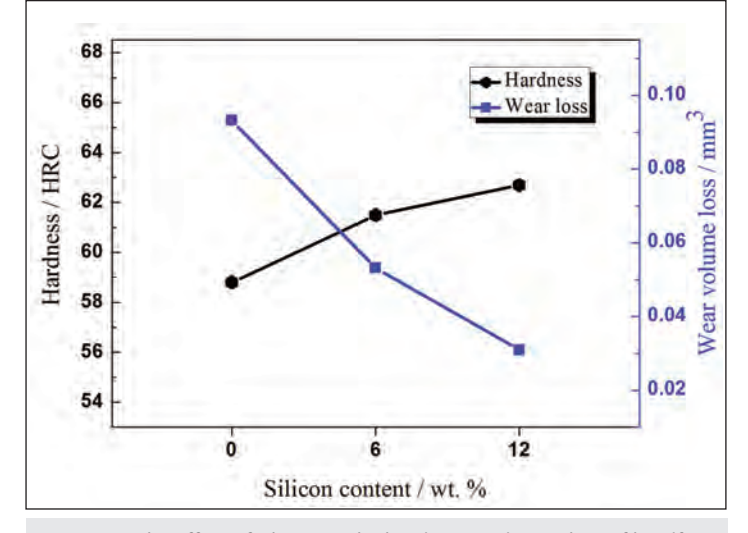


Fig. 12 — The effect of silicon on the hardness and wear loss of hardfacing alloys.

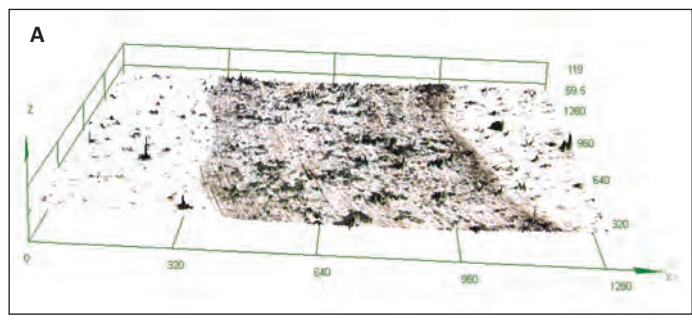
crease the level of silicon in the matrix. Solid solution of silicon also enhanced hardness. For these reasons, the wear loss of the alloy with 12 wt-% silicon was the smallest among all the alloys owing to the higher hardness and refinement of the microstructure.

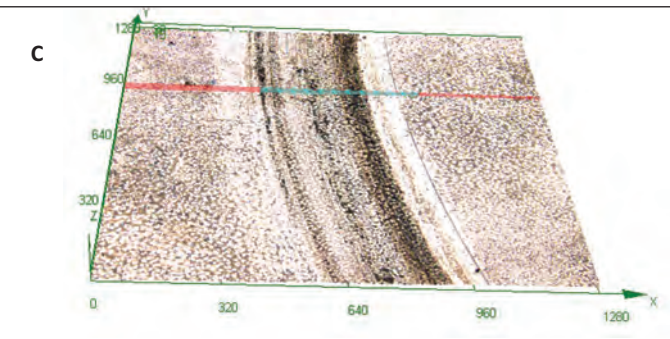
### Conclusions

A new type of silicon-added, slag-free, self-shielded fluxcored wire was developed. Silicon had a

high affinity for oxygen and was easily oxidized to change the pore formation tendency, and the residual silicon element affected the microstructure during the following solidification process. Based on the results, the following conclusions can be drawn:

- 1) Silicon up to 12 wt-% reduced the formation of the CO gas, resulting in the absence of the weld pool boiling, thus leading to weld porosity.
- 2) The Si-free hardfacing alloy displayed a typical hypereutectic microstructure that consisted of primary hexagonal-shaped  $M_7(C,B)_3$  and eutectic colonies of  $M_3(C,B)$  plus austenite. With increase in the amount of Fe-Si additive, the primary  $M_7(C,B)_3$  carbides gradually refined and became more uniform. The ferrite was formed directly from the liquid in the silicon-added hardfacing alloy. Fe<sub>3</sub>Si was formed when the silicon concentration in the residual liquid reached a certain level (the alloy with 12 wt-% silicon additive).
- 3) The addition of silicon to ironbased hardfacing alloy improved the wear resistance owing to the higher





hardness and refinement of the microstructure. The wear loss of the alloy with 12 wt-% silicon was the smallest among all the alloys.

4) The iron-based, slag-free, self-shielded flux-cored wire offered the best combination of the properties when 12 wt-% silicon was added into the core.

### Acknowledgments

This work was supported by Funding of National Natural Science Foundation of China (Grant No. 51405208), Open Research Fund of Provincial Key Laboratory of Advanced Welding Technology of Jiangsu University of Science and Technology (Grant No. JSAWT-14-03), Foundation for Scientists of Jiangsu University of Science and Technology (Grant No. 635061312), and a Project Funded by the Priority Academic Program Development of Jiangsu Higher Education Institutions.

### References

- 1. Zhou, Y. F., Yang, Y. L., Li, D., et al. 2012. Effect of titanium content on microstructure and wear resistance of Fe-Cr-C hardfacing layers. *Welding Journal* 91(8): 229-s to 235-s.
  - 2. Chang, C. M., Chen, Y. C., and Wu, W.

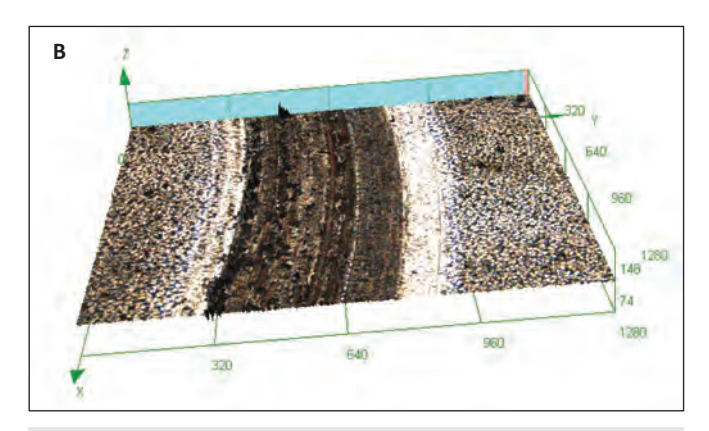


Fig. 14 — The macromorphology of the worn surface of hardfacing alloys with different silicon additions: A — 0 wt-%; B — 6 wt-%; C — 12 wt-%.

2010. Microstructural and abrasive characteristics of high carbon Fe-Cr-C hardfacing alloy.

Tribology International 43(5): 929–934.

3. Yüksel, N., and Şahin, S. 2014. Wear behavior-hardness-microstructure relation of Fe-Cr-C and Fe-Cr-C-B based hardfacing alloys. *Materials & Design* 58: 491–498.

4. Zhi, X. H., and Wang, J. X. 2014. Effect of niobium on primary carbides of hypereutectic high chromium cast iron. *Ironmaking and Steelmaking* 41(5): 394–399.

5. Hajihashemi, M., Shamanian, M., and Azimi, G. 2014. Physical, mechanical, and dry sliding wear properties of Fe-Cr-WC hardfacing alloys under different tungsten addition. *Metallurgical and Materials Transactions B*, pp. 1–9.

6. Zhou, Y. F., Yang, Y. L., Jiang, Y. W., et al. 2012. Fe-24 wt.%Cr-4.1 wt.%C hard-facing alloy: Microstructure and carbide refinement mechanisms with ceria additive. *Materials Characterization* 72: 77–86.

7. Buchely, M. F., Gutierrez, J. C., Leon, L. M., et al. 2005. The effect of microstructure on abrasive wear of hardfacing alloys. *Wear* 259(1): 52–61.

8. Kirchgaßner, M., Badisch, E., and Franek, F. 2008. Behaviour of iron-based hardfacing alloys under abrasion and impact. *Wear* 265(5): 772–779.

9. Jiang, M., Li, Z. X., Wang, Y. J., et al. 2008. Effect of vanadium on microstructures and properties of Fe-Cr-C self-shielded metal cored hardfacing alloys. *Science and Technology of Welding & Joining* 13(2): 114–117

10. Francis, J. A., Bednarz, B., and Bee, J. V. 2002. Prediction of steady state dilution in multipass hardfacing overlays deposited by self shielded flux cored arc welding. Science and Technology of Welding & Joining 7(2): 95–101.

11. Wang, Y., Li, S., Pan, C., et al. 2006. Development of the high-chromium cast iron flux cored wire for self-shielded. *Powder Metallurgy Industry* 16(3): 14.

12. Narayanan, B. K., Kovarik, L., Sarosi, P. M., et al. 2010. Effect of microalloying on precipitate evolution in ferritic welds and implications for toughness. *Acta Materialia* 58(3): 781–791.

13. Patrick, C. W., and Newell, W. F. 2014. Understanding welding cost: Using flux-cored arc welding (FCAW) for cost reduction and productivity improvement. ASME 2014 Pressure Vessels and Piping Conference. New York, N.Y.: American Society of Mechanical Engineers.

14. Liu, D. S., Liu, R. P., and Wei, Y. H. 2012. Effects of titanium additive on microstructure and wear performance of iron-based slag-free self-shielded flux-cored wire. *Surface and Coatings Technology* 207: 579–586.

15. Liu, D. S., Liu, R. P., Wei, Y. H., et al. 2013. Microstructure and wear properties of Fe-15Cr-2.5Ti-2C-xB wt.% hardfacing alloys. *Applied Surface Science* 271: 253–259.

16. Liu, D. S., Liu, R. P., and Wei, Y. H. 2014. Influence of tungsten on microstructure and wear resistance of iron base hard-facing alloy. *Materials Science and Technology* 30(3): 316–322.

17. Atamert, S., and Bhadeshia, H. K. D. H. 1988. *Proceedings of International Conference on Heat Treatment '87*. London, UK: Institute of Metals. pp. 39–43.

18. Il' inskii, A., Ślyusarenko, S., Slukhovskii, O., et al. 2002. Structural properties of liquid Fe-Si alloys. *Journal of Non-Crystalline Solids* 306: 90–98.

19. Azimi, G., and Shamanian, M. 2010. Effect of silicon content on the microstructure and properties of Fe-Cr-C hardfacing alloys. *Journal of Materials Science* 45: 842–849.